Noname manuscript No.
(will be inserted by the editor)

Speed Switch in Glioblastoma Growth Rate due to Enhanced Hypoxia-Induced Migration

Lee Curtin · Andrea Hawkins-Daarud · Kristoffer G. van der Zee · Kristin R. Swanson · Markus R. Owen

Received: date / Accepted: date

Abstract We analyze the wave-speed of the Proliferation Invasion Hypoxia Necrosis Angiogenesis (PIHNA) model that was previously created and applied to simulate the growth and spread of glioblastoma (GBM), a particularly aggressive primary brain tumor. We extend the PIHNA model by allowing for different hypoxic and normoxic cell migration rates and study the impact of these differences on the wave-speed dynamics. Through this analysis, we find key variables that drive the outward growth of the simulated GBM. We find a minimum tumor wave-speed for the model; this depends on the migration and proliferation rates of the normoxic cells and is achieved under certain conditions on the migration rates of the normoxic and hypoxic cells. If the hypoxic cell migration rate is greater than the normoxic cell migration rate above a threshold, the wave-speed increases above the predicted minimum. This increase in wave-speed is explored through an eigenvalue and eigenvector analysis of the linearized PIHNA model, which yields an expression for this threshold. The PIHNA model suggests that an inherently faster-diffusing hypoxic cell population can drive the outward growth of a GBM as a whole, and that this effect is more prominent for faster proliferating tumors that recover relatively slowly from a hypoxic phenotype. The findings presented here act as a first step in enabling patient-specific calibration of the PIHNA model.

Keywords glioblastoma · hypoxia · PIHNA · wave-speed · tumor growth

L. Curtin
Precision Neurotherapeutics Innovation Program, Mayo Clinic, Arizona, 85054
Tel.: +1 480-342-3930
E-mail: curtin.lee@mayo.edu

A. Hawkins-Daarud
Precision Neurotherapeutics Innovation Program, Mayo Clinic, Arizona, 85054

K.G. van der Zee
School of Mathematical Sciences, University of Nottingham, UK

K.R. Swanson
Precision Neurotherapeutics Innovation Program, Mayo Clinic, Arizona, 85054

M.R. Owen
School of Mathematical Sciences, University of Nottingham, UK

1 Introduction

Glioblastoma (GBM) is the highest grade of glioma from the World Health Organization [14]. It is uniformly fatal with an average survival time from diagnosis of only 15 months with standard of care treatment [24]. The standard therapy regime for this disease is a combination of resection, radiation and chemotherapy [24,25]. Magnetic Resonance Imaging (MRI) is the standard imaging modality for GBMs and is used routinely to monitor tumor growth and development throughout the progression of the disease. Different MRI sequences such as gadolinium-enhanced T1-weighted (T1Gd) and T2-weighted (T2) are used to identify the gross tumor volume. T1Gd shows gadolinium that has leaked into brain tissue, and T2 shows water that has done the same, which is known as edema. However, these MRI sequences together do not show a complete picture. Infiltrating tumor cells also exist beyond the resolution of these MRI sequences. In fact, malignant glioma cells have been cultured from histologically normal healthy tissue at a distance of 4cm from the gross tumor volume identified by MRI scans [21].

Hypoxia has been shown to induce more migration in glioma cells [12,36]. There is also evidence that glioma cells follow a dichotomy of migration and proliferation [7] and evidence of a lower proliferation marker for cells that exist in hypoxic regions of GBMs [5]. Tumors in hypoxic conditions release angiogenesis-promoting factors to encourage vessels to grow towards them and provide nutrients [8,13,37]. This process also occurs in normoxic conditions at a lower level [37]. Necrosis occurs in the vast majority of GBMs and presents in the core of the tumor [14]. Necrotic cells can lead to an unfavorable local microenvironment that injures nearby cells and subsequently spreads cell death [19,35].

Over the past 20 years, there have been many partial differential equation models that simulate GBM cell density and have provided various insights into this disease [10,15,16,26–29,29,31,32]. One such model is the Proliferation Invasion Hypoxia Necrosis Angiogenesis (PIHNA) model, which has been used to analyze the mechanistic properties of GBMs that lead to observed imaging features and has shown similar growth and progression patterns to those seen in patient tumors [31]. We carry out a traveling wave analysis on the PIHNA model to determine which parameters drive the outward growth of the tumor as a whole, and compare these analytical predictions with computational simulations in the cases of varying relative rates of migration between hypoxic and normoxic tumor cells. We find that the traveling wave dynamics only depend on the equations for the normoxic and hypoxic tumor cell densities. We find that the normoxic cell migration and proliferation rates, D_c and ρ, respectively, drive the minimum wave-speed in the PIHNA model, which is given by

$$s_{min} = 2\sqrt{D_c\rho}\left(1 - \frac{v_0}{K}\right) \tag{1}$$

and also depends on the initial background vasculature in the model, v_0, relative to the spatial carrying capacity, K. We find that s_{min} holds for published results using the PIHNA model as they have not allowed for different hypoxic cell and normoxic cell migration rates. We allow these migration rates to be different in the model and observe the effect of this variability on simulated tumor growth rates. We find that a faster-than-minimum wave-speed is achieved when hypoxic cells migrate sufficiently faster than normoxic cells and find a threshold above which

these dynamics can occur. This threshold depends on the proliferation rate ρ, the switching rate back from hypoxic cells to normoxic cells γ, and v_0/K. We denote this threshold k, and it is given by

$$k = 2 + \frac{\gamma}{\rho(1 - v_0/K)}. \tag{2}$$

These results are then confirmed and explored computationally through further model simulations. The PIHNA model therefore suggests that hypoxic cell migration, if sufficiently fast, is able to drive the outward growth of the tumor as a whole.

The PIHNA model has been used in various settings to explore possible mechanistic explanations for clinical observations of GBM [10,11,31]. It was built out of a much simpler model, the Proliferation Invasion (PI) model, a basic diffusion/logistic growth model whose simplicity has allowed for patient-specific calibration [27,28,30]. Despite its simplicity, the patient-specific calibration of the PI model has proven clinically prognostic for many aspects of clinical care [1–3,9,17, 18,22,32]. The increase in variables and parameters of the PIHNA model enables it to capture a wider range of clinical scenarios and questions, however, it has limited the ability for patient-specific calibration. The results presented here represent a first step in enabling patient-specific calibration of the PIHNA model as it shows the mathematical relationship between the wave speed and a handful of critical parameters, the same key relationship used to calibrate the PI model. Further, this relationship sheds light on expected tumor behavior based on the degree of aggressive hypoxia which is imageable through positron emission tomography (PET) scans, which, with further study, may influence clinical decision making.

We introduce the PIHNA model in the next section before calculating the expression for the minimum wave-speed in Section 3. In this section, we also find the threshold, k, on the relative migration between hypoxic and normoxic cells under which the minimum wave-speed is achieved. We then move onto PIHNA simulations in Section 4 to computationally validate our findings.

2 The PIHNA Model

The PIHNA model [31] simulates five different species and their interactions:

c - the density of normoxic tumor cells,
h - the density of hypoxic tumor cells,
n - the density of necrotic cells,
v - the density of vascular endothelial cells,
a - the concentration of angiogenic factors.

The dimensions of c, h, v and n are cells/mm^3 of tissue. The angiogenic factor, a, is a diffusing concentration with dimensions μmol/mm^3 tissue.

Normoxic cells proliferate with rate ρ and migrate with rate D_c, whereas hypoxic cells do not proliferate but migrate with rate D_h. Cells convert between normoxic and hypoxic phenotypes depending on the ability of the local vascular density to provide nutrients at their location; hypoxic cells in the model become

necrotic if they remain in such a region. When any other cell type meets a necrotic cell, they become necrotic with rate α_n. Previous publications on the PIHNA model have set the migration rate of hypoxic cells to be equal to that of normoxic cells, such that $D_h = D_c$. However, hypoxia has been shown to promote GBM cell migration, so we have allowed for this to be varied in the PIHNA model [12, 36].

Angiogenic factors are created by the presence of normoxic and hypoxic cells, decay naturally and are consumed through the creation and presence of vascular cells (v). Angiogenic factors are only consumed by vasculature and not tumor or necrotic cells. Necrotic cells are dead cells and their degradation is not considered in the model.

The governing partial differential equations for the PIHNA model are

$$\overbrace{\frac{\partial c}{\partial t}}^{\substack{\text{Rate of change}\\ \text{of normoxic}\\ \text{cell density}}} = \overbrace{\nabla\cdot(D_c(1-T)\nabla c)}^{\substack{\text{Net diffusion of}\\ \text{normoxic}\\ \text{glioma cells}}} + \overbrace{\rho c(1-T)}^{\substack{\text{Proliferation}\\ \text{of normoxic}\\ \text{glioma cells}}} + \overbrace{\gamma hV}^{\substack{\text{Conversion}\\ \text{of hypoxic}\\ \text{to normoxic}}} - \overbrace{\beta c(1-V)}^{\substack{\text{Conversion}\\ \text{of normoxic}\\ \text{to hypoxic}}} - \overbrace{\alpha_n\frac{nc}{K}}^{\substack{\text{Conversion}\\ \text{of normoxic}\\ \text{to necrotic}}}$$

$$\overbrace{\frac{\partial h}{\partial t}}^{\substack{\text{Rate of change}\\ \text{of hypoxic}\\ \text{cell density}}} = \overbrace{\nabla\cdot(D_h(1-T)\nabla h)}^{\substack{\text{Net diffusion of}\\ \text{hypoxic}\\ \text{glioma cells}}} - \overbrace{\gamma hV}^{\substack{\text{Conversion}\\ \text{of hypoxic}\\ \text{to normoxic}}} + \overbrace{\beta c(1-V)}^{\substack{\text{Conversion}\\ \text{of normoxic}\\ \text{to hypoxic}}} - \overbrace{\left(\alpha_h h(1-V) + \alpha_n\frac{nh}{K}\right)}^{\substack{\text{Conversion}\\ \text{of hypoxic}\\ \text{to necrotic}}}$$

$$\overbrace{\frac{\partial n}{\partial t}}^{\substack{\text{Rate of change}\\ \text{of necrotic}\\ \text{cell density}}} = \overbrace{\alpha_h h(1-V)}^{\substack{\text{Conversion}\\ \text{of hypoxic}\\ \text{to necrotic}}} + \overbrace{\alpha_n\frac{n(c+h+v)}{K}}^{\substack{\text{Contact necrosis}\\ \text{of all}\\ \text{living cells}}} \tag{3}$$

$$\overbrace{\frac{\partial v}{\partial t}}^{\substack{\text{Rate of change}\\ \text{of vascular}\\ \text{cell density}}} = \overbrace{\nabla\cdot(D_v(1-T)\nabla v)}^{\substack{\text{Net diffusion of}\\ \text{vasculature}}} + \overbrace{\mu\frac{a}{K_m+a}v(1-T)}^{\substack{\text{Net proliferation}\\ \text{of vasculature}}} - \overbrace{\alpha_n\frac{nv}{K}}^{\substack{\text{Conversion}\\ \text{of vasculature}\\ \text{to necrotic}}}$$

$$\overbrace{\frac{\partial a}{\partial t}}^{\substack{\text{Rate of change}\\ \text{of angiogenic}\\ \text{factor concentration}}} = \overbrace{\nabla\cdot(D_a\nabla a)}^{\substack{\text{Net diffusion of}\\ \text{angiogenic factor}}} + \overbrace{\delta_c c+\delta_h h}^{\substack{\text{Net production}\\ \text{of angiogenic factor}}} - \overbrace{q\mu\frac{a}{K_m+a}v(1-T)-\omega av}^{\substack{\text{Net consumption of}\\ \text{angiogenic factor}}} - \overbrace{\lambda a}^{\text{Decay}}$$

where

$$V = \frac{v}{v+c+h}, \tag{4}$$

and

$$T = (c+h+n+v)/K. \tag{5}$$

The term V models the relationship between the vasculature and its effect on the tumor. Note that V take values in $[0, 1]$ such that it affects the switching rates between the populations c, h and n. A value of $V(c, h, v) \approx 0$ corresponds to a very inefficient vasculature that cannot provide sufficient nutrients to the local tumor population; this would increase the conversion of normoxic cells to hypoxic cells and in turn necrotic cells. A high $V(c, h, v) \approx 1$ promotes a normoxic

	Definition	Value/Range	Units	Source
D_c	Diffusion rate of normoxic cells	$10-100$	$\frac{\text{mm}^2}{\text{year}}$	[9]
D_h	Diffusion rate of hypoxic cells	$(0.1-100)D_c$	$\frac{\text{mm}^2}{\text{year}}$	[9,15]*
ρ	Proliferation rate of normoxic cells	$10-100$	1/year	[9]
β	Switching rate from normoxia to hypoxia	0.1ρ	1/year	[31]
γ	Switching rate from hypoxia to normoxia	$0.005-0.5$	1/day	[31]*
α_h	Switching rate from hypoxia to necrosis	0.5β	1/year	[31]
α_n	Rate of contact necrosis	$\log(2)/50$	1/day	[20]
D_v	Diffusion rate of endothelial cells	0.18	$\frac{\text{mm}^2}{\text{year}}$	[31]
D_a	Diffusion rate of angiogenic factors	3.15	$\frac{\text{mm}^2}{\text{year}}$	[31]
δ_c	Normoxic cell production rate of angiogenic factors	2.77×10^{-13}	$\frac{\mu\text{mol}}{\text{cell}\times\text{year}}$	[31]
δ_h	Hypoxic cell production rate of angiogenic factors	5.22×10^{-10}	$\frac{\mu\text{mol}}{\text{cell}\times\text{year}}$	[31]
μ	Angiogenesis vasculature production rate	$\log(2)/15$	1/day	[31]
q	Consumption of angiogenic factors per cell	1.66	μmol/cell	[31]
λ	Natural decay rate of angiogenic factors	15.6	1/day	[31]
ω	Rate of removal of angiogenic factors by vasculature	λ/v_0	$\frac{1}{\text{cell}\times\text{year}}$	[31]
K	Maximal cell density	2.39×10^8	cells/cm^3	[31]

Table 1 Parameter definitions and values for the PIHNA model. A justification of parameters can be found in the supplementary material of [31]. *We have altered these rates in this formulation of PIHNA, which have not been changed previously.

phenotype. It is worth noting that, once necrotic cells are present in a simulation, they will always increase in population due to the contact necrosis in the model, which represents the injury of nearby cells and promotion of their necrosis. Further definitions can be found in Table 1.

The expression for T defined in Equation (5) is a spatiotemporal measure of the relative density of the cells in a region. It is used to limit growth and migration and used as a threshold to determine which densities would appear on different MRI sequences. Substituting the set of equations (3) into Equation (5) gives

$$K\frac{\partial T}{\partial t} = \nabla\cdot((1-T)(D_c\nabla c+D_h\nabla h+D_n\nabla n+D_v\nabla v))+(1-T)\left(\rho c+\frac{\mu a}{K_m+a}v\right),$$

from which it is clear that at $T=1$ the reaction and diffusion terms vanish, which implies T is restricted by the upper bound of 1 (as long as $T(x,0)\leq 1$). As T is a sum of non-negative components and $K>0$, we have that $T\geq 0$. Therefore, we have that $T\in[0,1]$ for sufficient initial conditions, for all x and $t\geq 0$.

Following the literature, we have assumed that a total relative cell density of at least 80% is visible on a T1Gd MRI, and a total relative density of at least 16% is visible on a T2 MRI [27,31]. In the PIHNA model, this translates to $T\geq 0.8$ being

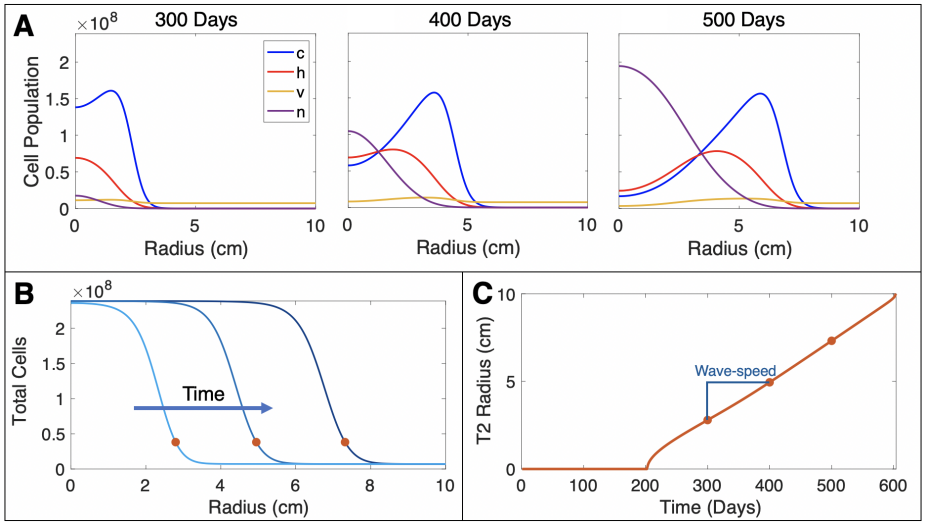

Fig. 1 (A) Three example time points (300 days, 400 days and 500 days) of a simulation with $D_c = 10^{1.5}\text{mm}^2/\text{year}$, $\rho = 10^{1.5}/\text{year}$, $\gamma = 0.05/\text{day}$ and $D_h/D_c = 10$. All cell types are shown and move outwards over time. Necrosis develops in the core of the tumor. (B) Total cells over time for the three time points shown in Subfigure A. The dots correspond to the T2 radius at each time point. (C) The T2 radius shown over time for the same simulation. This radial growth is non-linear for small tumor sizes, but settles to a linear rate, which is the wave-speed of the simulation.

visible on T1Gd MRI and $T \geq 0.16$ being visible on T2 MRI. By construction the T1Gd radius is always less than or equal to the T2 radius, which agrees with patient data [9].

For the purposes of the wave-speed calculations, we consider the PIHNA model in a one-dimensional spherically symmetric case with zero-flux boundary conditions at the end points, $r = 0$ and $r = r_{end}$. This does not take into account the full anatomy of the brain, but it is useful to gain insight into the behavior of the PIHNA model. The initial condition is given by

$$c(r, 0) = 1000e^{-100r^2}, \tag{6}$$

to simulate a small initiating population of normoxic tumor cells decreasing away from the core of the tumor. We also have $h(r, 0) = 0$, $n(r, 0) = 0$, $v(r, 0) = 0.03K$ and $a(r, 0) = 0$. We run the PIHNA simulations with the parameters found in Table 1.

In all simulations, the tumor and necrotic cell densities spread outwards. A peak in normoxic cell density leads and is followed by a peak in hypoxic cell density and then a zone of necrosis develops in the core of the tumor, as can be seen in Figure 1; this figure also shows how we calculate the wave-speed values from simulations.

3 Conditional Minimum Wave-speed for the PIHNA Model

In a similar fashion to the well-established minimum wave-speed of Fisher's Equation [6] that has been used for the PI tumor growth model [27], we carried out a wave-speed analysis to find an analytical expression for the tumor wave-speed in the PIHNA model. This wave-speed is what has enabled patient-specific calibration of the PI model for GBM patients, and we expect that this similar analysis will eventually allow for the patient-specific calibration of the PIHNA model as well. Note that in spherically symmetric coordinates, the wave-speed asymptotically approaches that of a planar wave-speed.

We start by linearizing the model ahead of the leading edge of the wave, that has the initial condition of $(c, h, n, v, a) = (0, 0, 0, v_0, 0)$; this gives an expression of

$$(c, h, n, v, a) = (0, 0, 0, v_0, 0) + (\hat{c}, \hat{h}, \hat{n}, \hat{v}, \hat{a}). \tag{7}$$

Substituting Equation (7) into the PIHNA model (Equation (3)) and discarding non-linear terms leads to the following set of equations:

$$\frac{\partial \hat{c}}{\partial t} = \nabla \cdot \left(D_c \left(1 - \frac{v_0}{K}\right) \nabla \hat{c} \right) + \rho \hat{c} \left(1 - \frac{v_0}{K}\right) + \gamma \hat{h} \tag{8}$$

$$\frac{\partial \hat{h}}{\partial t} = \nabla \cdot \left(D_h \left(1 - \frac{v_0}{K}\right) \nabla \hat{h} \right) - \gamma \hat{h} \tag{9}$$

$$\frac{\partial \hat{n}}{\partial t} = \alpha_n \hat{n} \frac{v_0}{K} \tag{10}$$

$$\frac{\partial \hat{v}}{\partial t} = \nabla \cdot \left(D_v \left(1 - \frac{v_0}{K}\right) \nabla \hat{v} \right) + \mu \frac{v_0}{K_m} \left(1 - \frac{v_0}{K}\right) \hat{a} - \alpha_n \frac{v_0}{K} \hat{n} \tag{11}$$

$$\frac{\partial \hat{a}}{\partial t} = \nabla \cdot (D_a \nabla \hat{a}) + \delta_c \hat{c} + \delta_h \hat{h} - q\mu \frac{v_0}{K_m} \left(1 - \frac{v_0}{K}\right) \hat{a} - \omega v_0 \hat{a} - \lambda \hat{a}, \tag{12}$$

where we have used $T = v_0/K$ and $V = 1$. The equations for $\hat{c}$ and $\hat{h}$ decouple from the system and it is these two equations that dictate the outward growth rate of the tumor. We will analyze these two equations to look for traveling wave solutions of the form

$$(\hat{c}, \hat{h}) = (\bar{c}, \bar{h}) \exp(\lambda(r - st)), \tag{13}$$

where s is the wave-speed. Substituting Equation (13) into Equations (8)-(9), gives rise to the following equations

$$-s\lambda \bar{c} = D_c \left(1 - \frac{v_0}{K}\right) \lambda^2 \bar{c} + \rho \left(1 - \frac{v_0}{K}\right) \bar{c} + \gamma \bar{h} \tag{14}$$

$$-s\lambda \bar{h} = D_h \left(1 - \frac{v_0}{K}\right) \lambda^2 \bar{h} - \gamma \bar{h} \tag{15}$$

Looking for non-trivial solutions to this system of equations yields eigenvalues as functions of the wave-speed, s. We have four eigenvalues, given by

$$\lambda_{1,2} = \frac{-s \pm \sqrt{s^2 - 4D_c\rho\left(1 - \frac{v_0}{K}\right)^2}}{2D_c\left(1 - \frac{v_0}{K}\right)} \text{ and } \lambda_{3,4} = \frac{-s \pm \sqrt{s^2 + 4D_h\gamma\left(1 - \frac{v_0}{K}\right)}}{2D_h\left(1 - \frac{v_0}{K}\right)}.$$

We have also found the corresponding eigenvectors for all of our eigenvalues, which we shall denote V_i for each λ_i. These are given by the following expressions, up to a proportional constant:

$$V_{1,2} = \begin{bmatrix} 1 \\ 0 \\ 0 \end{bmatrix} \text{ and } V_{3,4} = \begin{bmatrix} -\gamma \\ s\lambda_{3,4} + (D_c\lambda_{3,4}^2 + \rho)\left(1 - \frac{v_0}{K}\right) \\ 0 \end{bmatrix}. \tag{16}$$

The terms $\lambda_{1,2}$ are both negative as $s > 0$ by assumption. Due to positive restrictions on the state space (negative populations do not make any biological sense), a spiral approach around the point $(0, 0, 0, v_0, 0)$ cannot occur. Therefore, we need the discriminant of the set of quadratic $\lambda_{1,2}$ solutions to be greater than or equal to zero. In other words,

$$s^2 - 4D_c\rho\left(1 - \frac{v_0}{K}\right)^2 \geq 0. \tag{17}$$

Therefore, we have a minimum wave-speed of

$$s_{min} = 2\sqrt{D_c\rho}\left(1 - \frac{v_0}{K}\right). \tag{18}$$

There is no minimum wave-speed associated with the eigenvalues $\lambda_{3,4}$.

The PIHNA model will follow this minimum wave-speed if the eigenvalue λ_1 evaluated at this minimum gives the smallest possible negative eigenvalue of $\lambda_{1,2,3,4}$. If there exists some $s > s_{min}$ such that $0 > \lambda_i(s) > \lambda_1(s_{min})$ for some $i = 1, 2, 3, 4$, we will see the emergence of a solution with a larger wave-speed. In this section we will compute a threshold below which the minimum wave-speed is achieved but above which other dynamics may emerge.

We will call each eigenvalue evaluated at s_{min}, λ_i^{min}, for $i = 1, \ldots, 4$. We start by noting that $\lambda_2 \leq \lambda_1$ and $\lambda_3 > 0$, so neither of those can be negative with a smaller magnitude than λ_1^{min} to change the PIHNA wave-speed dynamics. As λ_4 becomes less negative for increasing values of D_h, there is a threshold value of D_h/D_c that leads to $\lambda_1^{min} = \lambda_1 = \lambda_4^{min}$ for which the minimum wave-speed is still achieved. For values of D_h/D_c that are smaller than this threshold, the minimum wave-speed will still be achieved. However, larger values of D_h/D_c may lead to a faster wave-speed, as the eigenvalues become smaller than λ_1^{min}. We have

$$\lambda_1^{min} = \frac{-s_{min} + \sqrt{s_{min}^2 - 4D_c\rho\left(1 - \frac{v_0}{K}\right)^2}}{2D_c\left(1 - \frac{v_0}{K}\right)}, \text{ and} \tag{19}$$

$$\lambda_4^{min} = \frac{-s_{min} - \sqrt{s_{min}^2 + 4D_h\gamma\left(1 - \frac{v_0}{K}\right)}}{2D_h\left(1 - \frac{v_0}{K}\right)}. \tag{20}$$

Setting $\lambda_1^{min} = \lambda_4^{min}$ and using the expression for s_{min} (Equation (18)) leads to

$$\lambda_1^{min} = \sqrt{\frac{\rho}{D_c}} = \frac{\sqrt{D_c\rho} + \sqrt{D_c\rho + D_h\gamma/(1 - v_0/K)}}{D_h} = \lambda_4^{min}. \tag{21}$$

Solving for D_h/D_c gives the non-trivial solution

$$\frac{D_h}{D_c} = 2 + \frac{\gamma}{\rho(1 - v_0/K)}. \tag{22}$$

We will define this threshold of D_h/D_c as k. Note that as $v_0 \leq K$, $k \geq 2$. So for the faster wave-speeds to occur, the hypoxic cell migration rate needs to be at least twice as fast as the normoxic cell migration rate. For $D_h/D_c = 1$, as is the case in previous PIHNA publications, we do not expect faster wave-speeds to occur, regardless of other simulation parameters.

4 Simulation Results

To calculate the simulated wave-speed in numerical simulations, we thresholded the total cell density at $T = 0.16$, which is a commonly assumed cell density threshold for visible tumor-related abnormalities on T2 MRI [27]. Following the establishment of a wave front, the simulated wave-speed levels out to a fixed value, see Figure 1. We analyze the wave-speed of large tumors to ensure we are analyzing established wavefronts while minimizing numerical error. We are particularly interested in the effect on the wave-speed of varying hypoxic cell migration rates, more specifically the change in their migration rate compared with normoxic cells (D_h/D_c), which has been allowed to vary in the PIHNA model for the first time. We also want to observe the effect of the D_h/D_c threshold, k, that allows for faster wave-speeds. Although we have already observed that the equations for the normoxic and hypoxic cell densities decouple in the linearized form of the PIHNA model, simulations presented here are for the full PIHNA model. Numerical simulations are run on a spherically symmetric domain, with a step size of 0.01mm. All simulations were run in Matlab 2018a using the inbuilt solver *pdepe.m*.

4.1 Relatively Fast Hypoxic Cell Diffusion Rates Increase Wave-speed

The wave-speed for PIHNA simulations with $D_h/D_c \leq k$ converges towards s_{min}. However, if we compute the wave-speed for simulations where $D_h > kD_c$, we see that the wave-speed can be faster, and continues to increase for larger D_h/D_c values; an example of this can be seen in Figure 2. Computing the corresponding eigenvalues shows a change in behavior for values of $D_h/D_c > k$. We also plot k on Figure 2, in which case $k = 2.60$ (three significant figures). These values of D_c and ρ are biologically realistic and based on the mean of previous migration and proliferation rate estimates from the PI model applied to patient-specific MRI data [33].

From these observations and our analysis in Section 3, we can deduce that if the hypoxic cell migration is sufficiently faster than the normoxic cell migration (such that $D_h/D_c > k$), the hypoxic cell population drives the outward growth of the tumor in the PIHNA model. This behavior intuitively agrees with the biological cell movement patterns that the model is trying to capture; cells moving faster dominate the growth outwards as they search for nutrients.

Focusing on the eigenvectors corresponding to the least negative eigenvalues, V_1 and V_4, we see that they influence the dynamics of the model. By plotting the normoxic cell density across space against the hypoxic cell density across space for a fixed time point where each simulation has converged to a stable wave-speed, together with V_1 and V_4, we can see how the traveling wave trajectory approaches the state ahead of the wave front. We present two simulations with

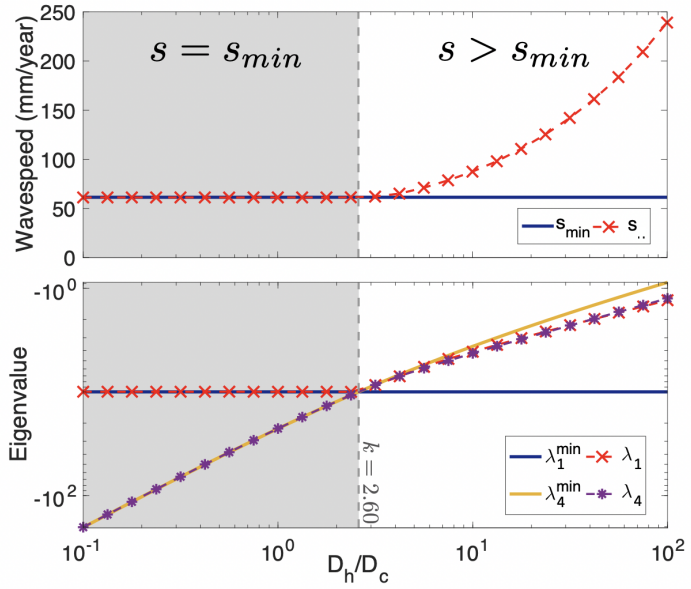

Fig. 2 As D_h/D_c is increased with $D_c = 10^{1.5}\text{mm}^2/\text{year}$, $\rho = 10^{1.5}/\text{year}$ and $\gamma = 0.05/\text{day}$, we see an increase in the converged numerical wave-speed past the threshold on D_h/D_c of $k = 2.60$. Wave-speeds taken as the average speed between 8 and 8.5cm of growth on simulated T2 MRI (16% total cell density threshold).

their corresponding V_1 and V_4 eigenvectors in Figure 3, one for $D_h/D_c = 10^{-1}$ and another for $D_h/D_c = 10^1$. For $D_h/D_c = 10^{-1}$, where the wave-speed follows the predicted minimum value, we see that the model approaches along $(c, h) = (0, 0)$ along the eigenvector V_1, whereas for $D_h/D_c = 10^1$, the approach is along V_4. In the linearized regime, we expect that $\hat{c} = \bar{c}\exp(\lambda(r - st))$, such that

$$\frac{\partial(\log(c))}{\partial r} \sim \lambda. \tag{23}$$

To provide further evidence concerning the traveling wave trajectory, we compared the gradient of the log of normoxic cells (c) with the eigenvalues λ_1 and λ_4. We see that for low values of D_h/D_c, the gradient more closely follows λ_1 and for large values of D_h/D_c, the gradient closely follows λ_4. We present examples of these results in the Appendix (Figure 6).

4.2 Low switching rate from hypoxia to normoxia, γ, amplifies wave-speed increase for large values of D_h/D_c

The switching rate from a normoxic cell to a hypoxic cell (β) is not present in the eigenvalues that dominate the behavior of the wave-speed, nor in the expression for k. We do however note that the switching rate from a hypoxic cell phenotype back to a normoxic cell phenotype, γ, is present in the expression for λ_4 (Equation (19)) and subsequently in the expression for the D_h/D_c threshold, k (Equation (22)).

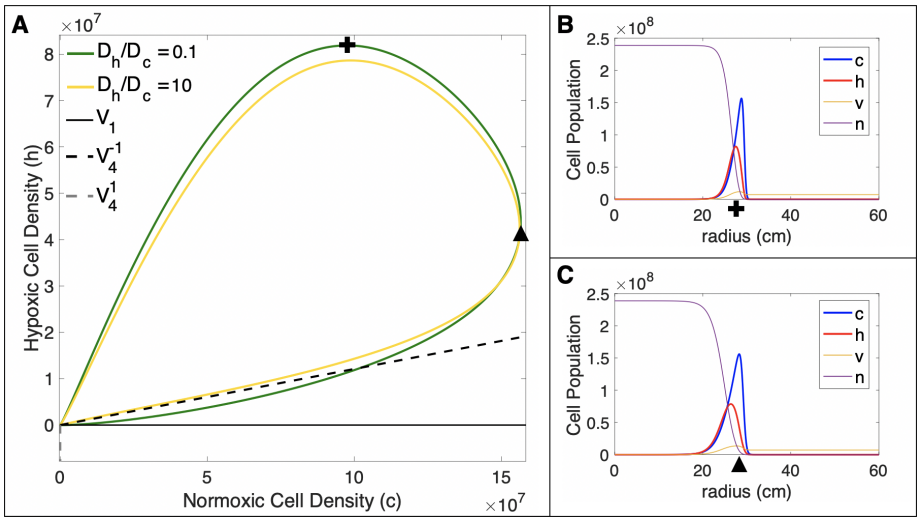

Fig. 3 (A) We show the normoxic and hypoxic cell densities across space for a fixed snapshot in time. For $D_h/D_c = 10^{-1}$, we see the dynamics follow V_1 near $(c, h) = (0, 0)$, which corresponds to the predicted minimum wave-speed, s_{min}. For $D_h/D_c = 10^1$, the dynamics have shifted towards V_4, corresponding with the faster numerical wave-speed we have observed. Here $D_c = 10^{1.5}\text{mm}^2/\text{year}$, $\rho = 10^{1.5}/\text{year}$. Eigenvectors and simulations are shown for large simulated T2 sizes, to ensure convergence of numerical eigenvectors (29.5 - 30cm T2 radius, with corresponding time points of 1421 and 1910 days for V_4). (B) The snapshot of the simulation with $D_h/D_c = 0.1$ used for subfigure A. The cross corresponds with the cross on subfigure A. (C) Corresponding snapshot with $D_h/D_c = 10$, with the triangle corresponding with the triangle on subfigure A.

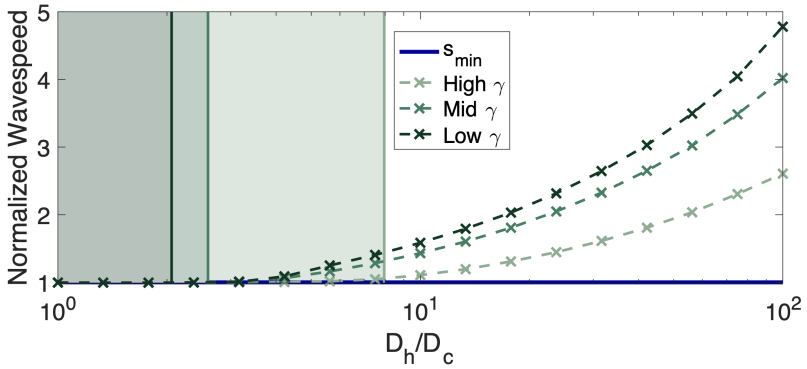

Fig. 4 As D_h/D_c is increased for varying γ values, we see an increase in the converged numerical wave-speed that is more pronounced for smaller values of γ; the corresponding thresholds k for wave-speeds faster than s_{min} are indicated. The values used are $\gamma = 0.005$, 0.05 and 0.5/day, with corresponding k values of 2.06, 2.60 and 7.95, respectively. Wave-speeds taken as the average speed between 8 and 8.5cm of growth on simulated T2 MRI (16% total cell density threshold) and presented relative to s_{min}.

We ran a similar set of simulations as in Section 4.1 with a higher value of $\gamma = 0.5$ and a lower value of $\gamma = 0.005$ to verify that the wave-speed increase, relative to s_{min}, would be affected for varying γ. As expected, higher values of γ increase k and correspond to a lower wave-speed for equivalent D_h/D_c values. We present these wave-speed results in Figure 4 where we also mark the corresponding values of k. For $\gamma = 0.005, 0.05$, and 0.5/day, we find $k = 2.06, 2.60$ and 7.95, respectively.

4.3 Wave-speed increase is more pronounced for faster-proliferating tumors

We also varied ρ to explore its effects on the increase in wave-speed for large values of D_h/D_c. We chose two more values of $\rho = 10^{1.25}$/year (lower ρ), and $\rho = 10^2$/year (higher ρ) and refer to the previous simulations with $\rho = 10^{1.5}$/year as a mid-range ρ. Throughout all simulations, we set $D_c = 10^{1.5}\text{mm}^2$/year and $\gamma = 0.05$/day, leading Equation (22) to give threshold values of $k = 2.19, 2.60$ and 3.06 for higher, medium and lower ρ simulations, respectively.

We present the wave-speeds normalized against their predicted values of s_{min} (Equation (18)) in order to compare the simulation results across different values of ρ. We see for values of D_h/D_c below their respective thresholds that the wave-speeds all follow their predicted minimum values. For simulations where D_h/D_c is above the respective threshold k, we see an increased wave-speed, as expected (see Figure 5). This relative increase in wave-speed is more pronounced for larger values of ρ. Simulated tumors with larger ρ values are also faster-growing tumors as they have a faster minimum wave-speed (Equation (18)).

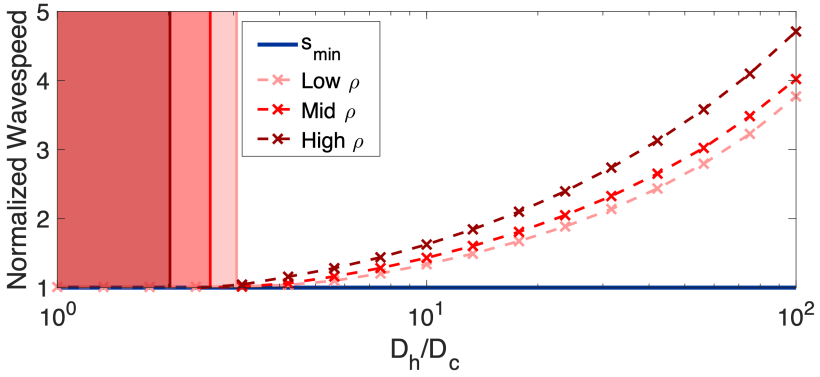

Fig. 5 As D_h/D_c is increased for varying D_c and ρ values, we see an increase in the relative wave-speed s/s_{min} that is more pronounced for larger values of ρ. The observed trend agrees with the expectation given by the corresponding values of k, which are also indicated. The values used are $\rho = 10^{1.25}$, $\rho = 10^{1.5}$ and 10^2/year, with corresponding k values of 2.19, 2.60 and 3.06, respectively. Wave-speeds taken as the average speed between 8 and 8.5cm of growth on simulated T2 MRI (16% total cell density threshold) and normalized against s_{min}.

5 Discussion

We have found an expression for the minimum wave-speed for the PIHNA model given by

$$s_{min} = 2\sqrt{D_c\rho}\left(1 - \frac{v_0}{K}\right) \tag{24}$$

and shown that this predicted wave-speed is attained when normoxic cell diffusion is greater than or equal to the diffusion of hypoxic cells. We therefore have shown that the predicted minimum wave-speed is valid for previous publications of the PIHNA model [31]. However, due to the *in vitro* evidence indicating that hypoxia can increase migration [12,36], we are interested in increasing the migration rate of hypoxic cells compared with normoxic cells in our extension of the PIHNA model. In the case that the hypoxic cells diffuse sufficiently faster than the normoxic cells, we see that the outward growth of the tumor is faster than the predicted minimum wave-speed value. In fact, we have quantified the value at which these faster rates of growth can occur through the threshold

$$k = 2 + \frac{\gamma}{\rho(1 - v_0/K)} \tag{25}$$

and note that the hypoxic cell diffusion has to be at least twice as fast as the normoxic cell diffusion. The threshold of hypoxic to normoxic cell migration rates is increased if the hypoxic cells can easily convert back to normoxia, and decreased for faster proliferating normoxic cell populations. This result suggests that faster-proliferating tumors that can only slowly recover from hypoxia are pushed to grow even faster by a highly migratory hypoxic subpopulation, more so than slower-proliferating tumors that can easily recover from hypoxia. The γ parameter encoding this recovery from hypoxia is the inherent ability of hypoxic tumor cells to adapt to a nutrient-rich microenvironment, switch off any hypoxia-related processes and reinitiate those related to a normoxic cell phenotype. This change in microenvironment is represented through the spatial variation in vasculature as the simulated tumors grow. As hypoxic cells migrate (in some cases faster than normoxic cells) they reach regions of more abundant vasculature and convert back to a normoxic phenotype. This recovery from hypoxia would likely also be influential in model dynamics if an initial condition of varying vasculature or treatment effects such as ischemia were introduced into the PIHNA model. The behavior of the PIHNA model suggests that limiting the lasting impact of hypoxia on phenotypic expression may slow the outward growth of GBM as would decreasing the motility of hypoxic tumor cells. Similarly, decreasing the motility and proliferation rates of normoxic cells would decrease the minimum wave-speed, the latter of which is already a widely exploited treatment mechanism through chemotherapy and radiation.

Of course the spherical symmetry assumed in the model does not fully capture the complex heterogeneity present in GBM. Inherent differences in vasculature and nutrient abundance are present in the healthy human brain [34] and spatial heterogeneity in hypoxia is observed in GBM [4,23]. Genetic differences within GBM could drive heterogeneity in all of the tumor-related parameters influencing the PIHNA wave-speed. This environmental and genetic heterogeneity could lead to varying wave-speeds of GBM growth within individual tumors. Even so, we anticipate eventual patient-specific calibration of this model to provide better

clinical insights into individual tumor behaviors beyond what the PI model can do. As quantification of aggressive hypoxic volumes becomes more readily available through PET scans, we anticipate this wave-speed estimate to play a critical role in estimating patient-specific parameters for this model.

The analysis presented here shows that the wave-speed dynamics do not depend on the vascular efficiency term, V, as long as $V = 1$ in its linearized form. We also do not see a dependence on the switching rate from the normoxic cell density to the hypoxic cell density, β. All of the results presented here are dictated by the equations for normoxic cell density and hypoxic cell density due to their independence from the other three equations in the linearized model. Necrosis, angiogenesis and vascular growth dynamics play no role in the outward growth rate in the PIHNA model. We have shown that this is the case both through theory and model simulations. This concept would hold for similar tumor growth models that decouple in their linearized forms and have different motilities between hypoxic and normoxic cell phenotypes.

Mathematically, the increase in simulated wave-speed corresponds to a change in the asymptotic traveling wave trajectory as D_h/D_c is increased, which causes an eigenvector associated with the hypoxic cell density characteristics to dominate the behavior of the PIHNA model. Biologically, this suggests that the faster migration of hypoxic cells can drive the growth of the whole tumor, as they migrate towards nutrient-rich environments and convert back to normoxic cells. If this conversion rate is high, the model suggests that the outward growth rate of the whole tumor is lower. The model does not predict that the wave-speed is affected by the proportions of hypoxic and normoxic cells. However, a reduction in vasculature ahead of the wave (v_0) does increase the invasion speed of the tumor due to the appearance of v_0 in the minimum predicted wave-speed. It would be interesting in future work to see how including a normal cell density affects these dynamics.

Acknowledgements

The authors gratefully acknowledge funding from the National Cancer Institute (U54CA193489) and the School of Mathematical Sciences at the University of Nottingham.

A Appendix

As discussed in the main body of this work, we wanted to show that our PIHNA simulations were following different eigenvalues depending on the value of D_h/D_c. In the linearized regime ahead of the wave, we expect that $\hat{c} = \bar{c}\exp(\lambda(x - st))$, such that

$$\frac{\partial(\log(c))}{\partial r} \sim \lambda. \tag{26}$$

In Figure 6 we present simulations at a T2 radius of 30cm. We see for the simulation with $D_h/D_c = 0.1$, $\partial(\log(c))/\partial r$ follows λ_1 ahead of the traveling wave, whereas for $D_h/D_c = 10$, $\partial(\log(c))/\partial r$ follows λ_4.

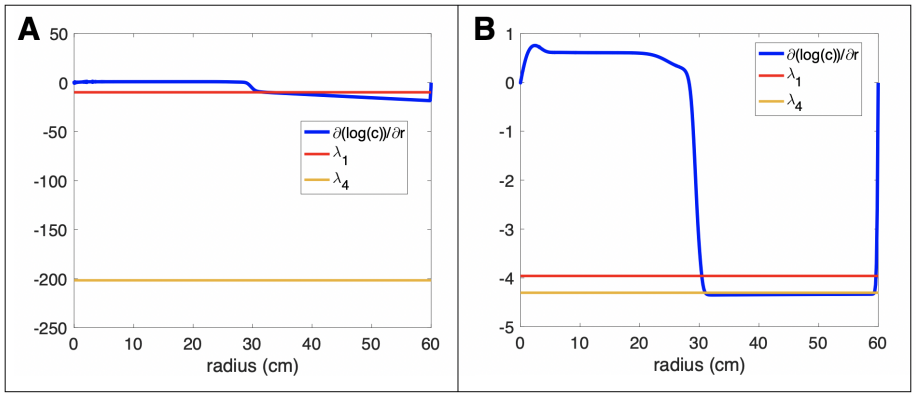

Fig. 6 The gradient of the log of the normoxic cells is plotted for a T2 radius of 30cm. As described in the main text, the leading edge of this simulated gradient (ignoring boundary effects present close to the edge of the domain) should follow the eigenvalue that controls the dynamics of the PIHNA model. Simulations presented here correspond with those presented in Figure 3. The simulation with $D_h/D_c = 0.1$ agrees more closely with λ_1, whereas the simulation with $D_h/D_c = 10$ follows λ_4. The results of these support the eigenvalue and eigenvector analysis in the main body of this work.

References

1. Jennifer E Adair, Sandra K Johnston, Maciej M Mrugala, Brian C Beard, Laura A Guyman, Anne L Baldock, Carly A Bridge, Andrea Hawkins-Daarud, Jennifer L Gori, Donald E Born, et al. Gene therapy enhances chemotherapy tolerance and efficacy in glioblastoma patients. *The Journal of clinical investigation*, 124(9):4082–4092, 2014.
2. Anne L Baldock, Sunyoung Ahn, Russell Rockne, Sandra Johnston, Maxwell Neal, David Corwin, Kamala Clark-Swanson, Greg Sterin, Andrew D Trister, Hani Malone, et al. Patient-specific metrics of invasiveness reveal significant prognostic benefit of resection in a predictable subset of gliomas. *PLoS One*, 9(10), 2014.
3. Anne L Baldock, Kevin Yagle, Donald E Born, Sunyoung Ahn, Andrew D Trister, Maxwell Neal, Sandra K Johnston, Carly A Bridge, David Basanta, Jacob Scott, et al. Invasion and proliferation kinetics in enhancing gliomas predict idh1 mutation status. *Neuro-oncology*, 16(6):779–786, 2014.
4. Christopher Bell, Nicholas Dowson, Mike Fay, Paul Thomas, Simon Puttick, Yaniv Gal, and Stephen Rose. Hypoxia imaging in gliomas with 18f-fluoromisonidazole pet: toward clinical translation. In *Seminars in nuclear medicine*, volume 45, pages 136–150. Elsevier, 2015.

5. D.J. Brat, A.A. Castellano-Sanchez, S.B. Hunter, M. Pecot, C. Cohen, E.H. Hammond, S.N Devi, B. Kaur, and E.G. Van Meir. Pseudopalisades in glioblastoma are hypoxic, express extracellular matrix proteases, and are formed by an actively migrating cell population. *Cancer Research*, 64(3):920–927, 2004.
6. R.A. Fisher. The wave of advance of advantageous genes. *Annals of Eugenics*, 7(4):355–369, 1937.
7. A. Giese, R. Bjerkvig, M.E. Berens, and M. Westphal. Cost of migration: invasion of malignant gliomas and implications for treatment. *Journal of Clinical Oncology*, 21(8):1624–1636, 2003.
8. J.D. Gordan and M.C. Simon. Hypoxia-inducible factors: central regulators of the tumor phenotype. *Current Opinion in Genetics & Development*, 17(1):71–77, 2007.
9. H.L.P. Harpold, E.C. Alvord, and K.R. Swanson. The evolution of mathematical modeling of glioma proliferation and invasion. *Journal of Neuropathology & Experimental Neurology*, 66(1):1–9, 2007.
10. A. Hawkins-Daarud, R.C. Rockne, A.R.A. Anderson, and K.R. Swanson. Modeling tumor-associated edema in gliomas during anti-angiogenic therapy and its impact on imageable tumor. *Frontiers in Oncology*, 3:66, 2013.
11. Andrea Hawkins-Daarud, Russell Rockne, David Corwin, Alexander RA Anderson, Paul Kinahan, and Kristin R Swanson. In silico analysis suggests differential response to bevacizumab and radiation combination therapy in newly diagnosed glioblastoma. *Journal of the Royal Society Interface*, 12(109):20150388, 2015.
12. M. Keunen, O.and Johansson, A. Oudin, M. Sanzey, S.A.A. Rahim, F. Fack, F. Thorsen, T. Taxt, M. Bartos, R. Jirik, et al. Anti-vegf treatment reduces blood supply and increases tumor cell invasion in glioblastoma. *Proceedings of the National Academy of Sciences*, 108(9):3749–3754, 2011.
13. P. Korkolopoulou, E. Patsouris, A.E. Konstantinidou, P.M. Pavlopoulos, N. Kavantzas, E. Boviatsis, I. Thymara, M. Perdiki, E. Thomas-Tsagli, D. Angelidakis, et al. Hypoxia-inducible factor 1α/vascular endothelial growth factor axis in astrocytomas. associations with microvessel morphometry, proliferation and prognosis. *Neuropathology and Applied Neurobiology*, 30(3):267–278, 2004.
14. D. Louis, H. Ohgaki, O. Wiestler, and W. Cavenee. *WHO Classification of Tumours of the Central Nervous System, Revised. Fourth Edition*. International Agency for Research on Cancer, 2016.
15. A. Martínez-González, G.F. Calvo, L.A.P. Romasanta, and V.M. Pérez-García. Hypoxic cell waves around necrotic cores in glioblastoma: a biomathematical model and its therapeutic implications. *Bulletin of Mathematical Biology*, 74(12):2875–2896, 2012.
16. S.C. Massey, M.C. Assanah, K.A. Lopez, P. Canoll, and K.R. Swanson. Glial progenitor cell recruitment drives aggressive glioma growth: mathematical and experimental modelling. *Journal of The Royal Society Interface*, page rsif20120030, 2012.
17. Maxwell Lewis Neal, Andrew D Trister, Tyler Cloke, Rita Sodt, Sunyoung Ahn, Anne L Baldock, Carly A Bridge, Albert Lai, Timothy F Cloughesy, Maciej M Mrugala, et al. Discriminating survival outcomes in patients with glioblastoma using a simulation-based, patient-specific response metric. *PloS one*, 8(1), 2013.
18. M.L. Neal, A.D. Trister, S. Ahn, A. Baldock, C. A Bridge, L. Guyman, J. Lange, R. Sodt, T. Cloke, A. Lai, et al. Response classification based on a minimal model of glioblastoma growth is prognostic for clinical outcomes and distinguishes progression from pseudoprogression. *Cancer Research*, 73(10):2976–2986, 2013.
19. Shaan M Raza, Frederick F Lang, Bharat B Aggarwal, Gregory N Fuller, David M Wildrick, and Raymond Sawaya. Necrosis and glioblastoma: a friend or a foe? a review and a hypothesis. *Neurosurgery*, 51(1):2–13, 2002.
20. A. Roniotis, V. Sakkalis, E. Tzamali, G. Tzedakis, M. Zervakis, and K. Marias. Solving the pihna model while accounting for radiotherapy. In *Advanced Research Workshop on In Silico Oncology and Cancer Investigation-The TUMOR Project Workshop (IARWISOCI), 2012 5th International*, pages 1–4. IEEE, 2012.
21. D.L. Silbergeld and M.R. Chicoine. Isolation and characterization of human malignant glioma cells from histologically normal brain. *Journal of Neurosurgery*, 86(3):525–531, 1997.
22. Kyle W Singleton, Alyx B Porter, Leland S Hu, Sandra K Johnston, Kamila M Bond, Cassandra R Rickertsen, Gustavo De Leon, Scott A Whitmire, Kamala R Clark-Swanson, Maciej M Mrugala, et al. Days gained response discriminates treatment response in patients with recurrent glioblastoma receiving bevacizumab-based therapies. *bioRxiv*, page 752402, 2019.

23. Alexander M Spence, Mark Muzi, Kristin R Swanson, Finbarr O'Sullivan, Jason K Rockhill, Joseph G Rajendran, Tom CH Adamsen, Jeanne M Link, Paul E Swanson, Kevin J Yagle, et al. Regional hypoxia in glioblastoma multiforme quantified with [18f] fluoromisonidazole positron emission tomography before radiotherapy: correlation with time to progression and survival. *Clinical Cancer Research*, 14(9):2623–2630, 2008.
24. R. Stupp, M.E. Hegi, W.P. Mason, M.J. van den Bent, M.J.B. Taphoorn, R.C. Janzer, S.K. Ludwin, A. Allgeier, B. Fisher, K. Belanger, et al. Effects of radiotherapy with concomitant and adjuvant temozolomide versus radiotherapy alone on survival in glioblastoma in a randomised phase iii study: 5-year analysis of the eortc-ncic trial. *The Lancet Oncology*, 10(5):459–466, 2009.
25. R. Stupp, W.P. Mason, M.J. Van Den Bent, M. Weller, B. Fisher, M.J.B. Taphoorn, K. Belanger, A.A. Brandes, C. Marosi, U. Bogdahn, et al. Radiotherapy plus concomitant and adjuvant temozolomide for glioblastoma. *New England Journal of Medicine*, 352(10):987–996, 2005.
26. A. Swan, T. Hillen, J.C. Bowman, and A.D. Murtha. A patient-specific anisotropic diffusion model for brain tumour spread. *Bulletin of Mathematical Biology*, 80(5):1259–1291, 2018.
27. K.R. Swanson. Mathematical modeling of the growth and control of tumors, 1999.
28. K.R. Swanson, E.C. Alvord, Jr, and J.D. Murray. A quantitative model for differential motility of gliomas in grey and white matter. *Cell Prolif*, 33(5):317–29, Oct 2000.
29. K.R. Swanson, C. Bridge, J.D. Murray, and E.C. Alvord. Virtual and real brain tumors: using mathematical modeling to quantify glioma growth and invasion. *Journal of the Neurological Sciences*, 216(1):1–10, 2003.
30. K.R. Swanson, C. Bridge, J.D. Murray, and E.C. Alvord, Jr. Virtual and real brain tumors: using mathematical modeling to quantify glioma growth and invasion. *Journal of the Neurological Sciences*, 216(1):1–10, Dec 2003.
31. K.R. Swanson, R.C. Rockne, J. Claridge, M.A.J. Chaplain, E.C. Alvord, and A.R.A. Anderson. Quantifying the role of angiogenesis in malignant progression of gliomas: in silico modeling integrates imaging and histology. *Cancer Research*, 71(24):7366–7375, 2011.
32. KR Swanson, RC Rostomily, and EC Alvord Jr. A mathematical modelling tool for predicting survival of individual patients following resection of glioblastoma: a proof of principle. *British journal of cancer*, 98(1):113–119, 2008.
33. Christina H Wang, Jason K Rockhill, Maciej Mrugala, Danielle L Peacock, Albert Lai, Katy Jusenius, Joanna M Wardlaw, Timothy Cloughesy, Alexander M Spence, Russ Rockne, et al. Prognostic significance of growth kinetics in newly diagnosed glioblastomas revealed by combining serial imaging with a novel biomathematical model. *Cancer research*, 69(23):9133–9140, 2009.
34. Tatsuo Yamaguchi, Iwao Kanno, Kazuo Uemura, Fumjo Shishido, A Inugami, Toshihide Ogawa, Matsutaro Murakami, and Kazuo Suzuki. Reduction in regional cerebral metabolic rate of oxygen during human aging. *Stroke*, 17(6):1220–1228, 1986.
35. Y Yang, Lin Hou, Y Li, J Ni, and L Liu. Neuronal necrosis and spreading death in a drosophila genetic model. *Cell death & disease*, 4(7):e723, 2013.
36. David Zagzag, Yevgeniy Lukyanov, Li Lan, M Aktar Ali, Mine Esencay, Olga Mendez, Herman Yee, Evelyn B Voura, and Elizabeth W Newcomb. Hypoxia-inducible factor 1 and vegf upregulate cxcr4 in glioblastoma: implications for angiogenesis and glioma cell invasion. *Laboratory Investigation*, 86(12):1221, 2006.
37. David Zagzag, Hua Zhong, Joanne M Scalzitti, Erik Laughner, Jonathan W Simons, and Gregg L Semenza. Expression of hypoxia-inducible factor 1α in brain tumors. *Cancer*, 88(11):2606–2618, 2000.